Dynamics of Defects in the Vector Complex Ginzburg-Landau Equation

Miguel Hoyuelos [a,b] , Emilio Hernández-García [a] , Pere Colet [a] and Maxi San Miguel [a]

[a] *Instituto Mediterráneo de Estudios Avanzados, IMEDEA (CSIC-UIB), Campus Universitat Illes Balears, E-07071 Palma de Mallorca, Spain.* [1]

[b] *Departamento de Física, Facultad de Ciencias Exactas y Naturales, Universidad Nacional de Mar del Plata, Funes 3350, 7600 Mar del Plata, Argentina*

Abstract

Coupled Ginzburg-Landau equations appear in a variety of contexts involving instabilities in oscillatory media. When the relevant unstable mode is of vectorial character (a common situation in nonlinear optics), the pair of coupled equations has special symmetries and can be written as a *vector complex Ginzburg-Landau equation*. Dynamical properties of localized structures of topological character in this vector-field case are considered. Creation and annihilation processes of different kinds of vector defects are described, and some of them interpreted in theoretical terms. A transition between different regimes of spatiotemporal dynamics is described.

Key words: Vector Ginzburg-Landau equation, topological defects, spatiotemporal chaos, optical instabilities, light polarization.

1 Introduction

Localized structures, objects with some kind of particle-like behaviour, can be found in a variety of non-linearly evolving fields. Examples are vortices in fluids, superfluids and superconductors, propagating pulses of excitation in nerve systems, solitary waves in chemical media, in parametrically driven surfaces, and in granular media, among others [1]. An understanding of complex evolving configurations can be sometimes achieved in terms of the interaction rules of the particle-like entities. In most cases, however, numerical integration

[1] `http://www.imedea.uib.es/PhysDept/`

of the evolution equations is the most powerful tool to investigate the role of the localized structures.

Nonlinear optical cavities have been specially prolific in providing examples of localized structures [2]. They appear in the tranverse profile of the field and can take the form of vortices, or of bright or dark dissipative spatial solitons. It is usually considered that the polarization degree of freedom of the electromagnetic field is fixed either by material anisotropies or by experimental arrangement. Thus the description of the dynamics is done in terms of a scalar field. However in the cases in which the polarization of the light is not fixed, the vector nature of the electromagnetic field leads to striking topological phenomena [3]. Recently reported examples of localized structures for which the polarization plays a fundamental role include points of zero amplitude in both components of the field in a periodic elliptically polarized background, found in type II OPO [4] and dots of low amplitude in a circularly polarized component of the field in an almost circularly polarized background found in self-defocusing vectorial Kerr resonators [5].

The scalar Complex Ginzburg-Landau (CGL) equation is considered a paradigm model for the qualitative description of general non-linear oscillatory media (see, for example, [6–8]). The vector complex Ginzburg-Landau (VCGL) equation [9–13] plays the same role when the order parameter is of vector character, as is the case for the electromagnetic field when the polarization is not fixed. For example, the VCGL equation is an appropriate model for laser emission from wide-aperture resonators close to the lasing threshold [13] in the absence of polarization-selecting cavity features. Different kinds of localized structures [9–12,14–16] are present in the dynamic states of the twodimensional VCGL equation. From a topological point of view, they are *defects*, that is, places where the field state departs from some basic ordered state. These objects carry topological properties which endorse them with a characteristic stability and robustness.

In this Paper we study the dynamical properties of these defects for several dynamical regimes of the VCGL equation. In addition to reviewing and adding details to results previously presented, which address the synchronization properties of spatiotemporally chaotic states [14], the identification of a transition from a *glass* to a *gas* phase [15], and the formation and annihilation processes leading to the different types of defects [16], we interpret some of these findings in terms of the stability properties of the waves emitted by the defect cores, and in terms of a recent perturbative analytic approach [17]. Since we are interested mostly in the dynamics of topological defects, we consider here just the twodimensional VCGL case, for which point defects are topologically stable. For VCGL dynamics in one spatial dimension we refer the reader to [18,14,19].

Section 2 presents the basic equations and properties. The different topological defects are described in Sect. 3, and Sect. 4 is devoted to their dynamical properties. A description of a *gas-like* phase is presented in Sect. 5. In Sect. 6 we briefly discuss a situation of phase separation. Finally (Sect. 7) we summarize our conclusions. The Appendix addresses the stability of waves emitted by vector defects.

2 The vector Complex Ginzburg-Landau equation

Extended systems close to a Hopf bifurcation at zero wavenumber are described by the CGL equation :

$$\partial_t A = A + (1 + i\alpha)\nabla^2 A - (1 + i\beta)|A|^2 A. \tag{1}$$

For systems where the relevant unstable mode is of vectorial character, Eq. (1) is generalized to the VCGL equation,

$$\partial_t \mathbf{A} = \mathbf{A} + (1 + i\alpha)\nabla^2 \mathbf{A} - (1 + i\beta)\left[(\mathbf{A}\cdot\mathbf{A}^*)\mathbf{A} + \frac{(\gamma-1)}{2}(\mathbf{A}\cdot\mathbf{A})\mathbf{A}^*\right]. \tag{2}$$

In the simplest case $\mathbf{A}$ has two complex components. This is precisely the case of optical systems, for which, $\mathbf{A} = (A_x, A_y)$ describe the complex slowly varying amplitude of the electric field, where A_x and A_y are the cartesian components. The right and left circularly polarized components (A_+, A_-) are related to them via the relations $A_x = (A_+ + A_-)/\sqrt{2}$ and $A_y = (A_+ - A_-)/(i\sqrt{2})$. In terms of the circular components, Eq. (2) reads

$$\partial_t A_\pm = A_\pm + (1 + i\alpha)\nabla^2 A_\pm - (1 + i\beta)(|A_\pm|^2 + \gamma|A_\mp|^2)A_\pm. \tag{3}$$

The coefficient γ, which in general can be complex, gives the coupling between the components. For $\gamma = 0$ we recover a pair of uncoupled equations of the form (1). We will often refer to Eq. (1) as the *scalar* CGL, to contrast it with Eqs. (2) or (3). For $\gamma \neq 0$, Eq. (3) can be thought as a particularly symmetric example (for example group velocity terms are absent) of a pair of coupled complex Ginzburg-Landau equations of the kind usually encountered in wave competition situations [6].

When Eq. (2) is derived for the Hopf bifurcation leading to laser emission[13], α is related to the strength of diffraction, and β to the nonlinear frequency detuning. In this case, the so called Benjamin-Feir stability criterion $1 + \alpha\beta > 0$ is always satisfied, which means that there are always some plane waves

which are stable against long wavelength perturbations. In addition, for laser systems, γ turns out to be a real parameter, and $\gamma > -1$. In this Paper, we will restrict our study to these ranges of parameters.

Equation (3) has a family of plane-wave solutions of the form:

$$A_\pm = Q_\pm e^{-i(\mathbf{k}_\pm.\mathbf{r}-\omega_\pm t+\phi_{0\pm})} \quad . \tag{4}$$

Within this family, the simplest solutions are the circularly polarized traveling waves, for which one of the components is identically zero:

$$Q_+ = 1-k^2, Q_- = 0, \omega_+ = -\beta + (\beta-\alpha)k^2 \tag{5}$$

or

$$Q_+ = 0, Q_- = 1-k^2, \omega_- = -\beta + (\beta-\alpha)k^2 \tag{6}$$

Within the family (4) there are also solutions in which both components coexist. For wavevectors with the same modulus, $k_+ = k_- = k$, we have

$$\begin{aligned} Q_+^2 &= Q_-^2 = Q^2 = \frac{1-k^2}{1+\gamma} \\ \omega_+ &= \omega_- = \omega = -\beta + (\beta-\alpha)k^2. \end{aligned} \tag{7}$$

We can have a linearly polarized traveling wave ($\mathbf{k}_+ = \mathbf{k}_-$) or a standing wave with periodic linear polarization ($\mathbf{k}_+ = -\mathbf{k}_-$). It is also possible to have depolarized solutions [13] with $k_+ \neq k_-$:

$$\begin{aligned} Q_\pm &= (1-\gamma+\gamma k_\pm^2 - k_\mp^2)/(1-\gamma^2) \\ \omega_\pm &= -\alpha k_\pm^2 - \beta(Q_\pm^2 + \gamma Q_\mp^2) \end{aligned} \tag{8}$$

The qualitative behavior for the VCGL equation (3) for $|\gamma| < 1$ is rather different from the one for $\gamma > 1$. In the second case the nonlinear competition between A_+ and A_- tends to favor one of them against the other, so that in regions where A_+ is developed, A_- generally vanishes, and viceversa. There are stable circularly polarized solutions of the form (5) or (6) while solutions of the form (7) which involve the coexistence of both fields are linearly unstable. On the contrary, for $|\gamma| < 1$, wave coexistence is generally achieved. Circularly polarized solutions of the form (5) or (6) are linearly unstable while there are stable solutions of the form (7) and (8). The character of the topological defects in both cases is different [11,12]. In Sects. 6-5 we will consider the case $|\gamma| < 1$. The case $\gamma > 1$ will be discussed in Sect. 6.

For γ real, the point in parameter space $\alpha = \beta = 0$ represents a special case of particularly simple dynamics. The VCGL equation becomes then a potential system, or more precisely [20,21], a 'relaxational gradient' dynamical system. Dynamics at long times approaches steady states that are identified as the minima of a Lyapunov potential. This is the case which is considered in greater detail in [11,12]. A more general situation is $\alpha = \beta$. In this case the system can be classified as 'relaxational non-gradient' [20,21], and although a Lyapunov functional can be still identified, the attractor for the dynamics is no longer steady in general. The limiting 'conservative case' $\alpha = \beta \to \infty$, also addressed in [11,12], leads to coupled nonlinear Schrödinger (or Gross-Pitaevskii) equations. This last limit is of great interest for the description of multicomponent Bose condensates [22] or the propagation of vector solitons in optical fibers [23].

3 Scalar and vector defects for $|\gamma| < 1$.

Starting from random initial conditions, even if the condition for existence of stable plane waves ($1 + \alpha\beta > 0$) is satisfied, solutions of (3) usually do not evolve to a simple plane wave (4) due to the presence of defects: points where the phase of A_+ or A_- is undefined and the corresponding amplitude is equal to zero. Around each defect, a spiral wave develops (except if $\alpha = \beta$) that, far from the defect core, approaches a plane wave with a particular wave number which has been dynamically selected by the presence of the defect. For example, Fig. 1 shows different views of a configuration obtained after time evolution [24] starting from random initial conditions, for $\alpha = 0.2$, $\beta = 2$, and $\gamma = 0.1$. The configuration consist of wave domains separated by shock waves. There is a defect in both components (the black dot) in the center of each domain. Inhomogeneities and defects in just one of the components have been expelled away from the defect core with a given group velocity.

Therefore, two different kinds of defects are readily identified: *Vector defects* are points at which the two components A_+ and A_- simultaneously vanish (and thus the same happens for A_x and A_y at the same point). *Scalar defects* (*mixed defects* in the nomenclature of [11,12]) are those at which only one of the two fields A_+ or A_- vanish. In this case the vector $\mathbf{A}$ is not zero, and the components A_x and A_y do not necessarily vanish, but they have still a singular topological structure to be described below. The following ansatz describes the field $\mathbf{A}$ close to a scalar or to a vector defect:

$$A_\pm(r,\theta) = R_\pm(r) e^{i\phi_\pm(r,\theta)}. \tag{9}$$

Where (r,θ) are the polar coordinates with the origin of coordinates at the

defect core. The amplitude of A_+ and (or) A_- go to zero at the core of a vector (scalar) defect: R_+ and (or) $R_- \to 0$ for $r \to 0$. The phase of the component which vanishes at $r = 0$ is

$$\phi_i(r,\theta) = n_i\theta + \psi_i(r) - \omega_i t + \phi_{0i} \ , \tag{10}$$

where the subindex i stands for $+$ or $-$. From expression (10), n_i is seen to satisfy

$$n_i = \frac{1}{2\pi} \oint_\Gamma \nabla\phi_i \cdot d\mathbf{r}, \tag{11}$$

where Γ is a closed path around the defect. This identifies n_i as the topological charge associated to the singularity in the field A_i. It necessarily takes integer values. In our numerical simulations we have never found for it a value different from 0, $+1$ or -1. ω_i is the rotation frequency of the spiral wave in A_i. For $r \to \infty$, $\psi_\pm(r) \to kr$.

It is possible to make a classification of defects using topological arguments [11,12]. Although this is not the way in which it was originally introduced, the classification becomes particularly simple in terms of the charges (11). As stated before, a *vector* defect is the one at which both components of the field vanish. Thus, necessarily both n_+ and n_- are nonvanishing. A vector defect is of type *argument* when the charges in the two field components have the same signs, i.e., when $n_+ = n_- = 1$ or $n_+ = n_- = -1$. If the charges are of opposite signs, i.e., when $n_+ = -n_- = 1$ or $n_+ = -n_- = -1$, the vectorial defect is of *director* type. A *scalar* defect is the one at which just one component of the field, but not the other, vanish. This implies that only one of the two charges is different from zero: $n_+ = \pm 1$ and $n_- = 0$, or $n_- = \pm 1$ and $n_+ = 0$ (see Fig. 2).

Numerically we observe that for vectorial defects both fields have identical modulus near the core: $|A_+| = |A_-|$, thus $R_+(r) = R_-(r) = R(r)$. Then close to a vector defect, Eq. (3) becomes

$$\partial_t A_\pm = A_\pm + (1 + i\alpha)\nabla^2 A_\pm - (1 + i\beta)(1 + \gamma)|A|^2_\pm A_\pm. \tag{12}$$

Each component is described by a scalar CGL equation (1) for a rescaled value of the common amplitude, $\tilde{A} \equiv \sqrt{1+\gamma}A_\pm$. In the rescaled variable, the shape and the size of the vectorial defect is independent of γ. Furthermore, we can use the arguments given by Hagan for the scalar CGL equation [25] to determine the wave numbers k_+ and k_-. According to this the spiral wavenumber depends only on the parameters α and β, therefore $k_+ = k_- = k_H$, where $k_H(\alpha,\beta)$ is the wavenumber of a spiral in the scalar CGL. Far from the defect core, as $r \to \infty$,

$\psi_+(r) = \psi_-(r) = \psi(r) \to k_H r$. The rotation frequencies are $\omega_+ = \omega_- = \omega$, where ω is given by Eq. (7) using $k = k_H$. It turns out [25] that the dependence of k_H on α and β is always through the combination

$$\kappa = \left| \frac{\alpha - \beta}{1 + \alpha\beta} \right| \ , \tag{13}$$

a parameter that will be important in the following. If $\kappa = 0$, $k_H = 0$, so that when $\alpha = \beta$ (the relaxational case) a homogeneous state is found instead of a wave far from the vector defect core.

For an argument vectorial defect, $n_+ = n_- = n = \pm 1$, and we have,

$$\begin{aligned} A_x &= \sqrt{2} R(r) \cos(\Delta\phi_0/2) e^{i[n\theta + \psi(r) - \omega t + (\phi_{0+} + \phi_{0-})/2]} \\ A_y &= \sqrt{2} R(r) \sin(\Delta\phi_0/2) e^{i[n\theta + \psi(r) - \omega t + (\phi_{0+} + \phi_{0-})/2]} \end{aligned} \ , \tag{14}$$

where $\Delta\phi_0 = \phi_{0+} - \phi_{0-}$ is the difference of initial phases of A_+ and A_-. If $\mathbf{A}$ represents an optical field, its polarization is linear, since the cartesian components A_x and A_y oscillate in phase. The angle of polarization is the constant $\xi = \Delta\phi_0/2$.

For a director vectorial defect, $n_+ = -n_- = n = \pm 1$, we have,

$$\begin{aligned} A_x &= \sqrt{2} R(r) \cos(n\theta + \Delta\phi_0/2) e^{i[\psi(r) - \omega t + (\phi_{0+} + \phi_{0-})/2]} \\ A_y &= \sqrt{2} R(r) \sin(n\theta + \Delta\phi_0/2) e^{i[\psi(r) - \omega t + (\phi_{0+} + \phi_{0-})/2]}. \end{aligned} \tag{15}$$

The polarization in this case is also linear at each point, but the angle of polarization, given by $\xi = n\theta + \Delta\phi_0/2$, rotates around the core of the defect (from here the name of *director* defect).

The defects just presented do indeed appear spontaneously in numerical simulations of Eq. (2) in appropriate parameter ranges. However, the classification by itself does not indicate much about the dynamics. It turns out that, when present, the vectorial defects dominate the dynamics, as shown in Fig. 1. They generate a large exclusion domain from which any inhomogeneity or scalar defect is expelled away. The scalar defects accumulate at the domain limits. The modulus of A_+ and A_- remain essentially frozen in time. The phases ϕ_+ and ϕ_- display corotating spirals for the argument defects and counterrotating spirals for the director defects, in agreement with (10) for the appropriate values of the charges n_i. We also show in Fig. 1 the global phase $\phi_g = \phi_+ + \phi_-$ and the relative phase $\phi_r = \phi_+ - \phi_-$. Argument and director defects are easily distinguished in the plot of the global phase: around an argument defect a two-armed spiral is formed (in a closed path around the defect ϕ_g changes in

4π), while a target pattern is seen in the domain of a director defect (ϕ_g does not change). The relative phase ϕ_r does not change in a closed path around an argument defect while for a director defect it changes in 4π. The scalar defects are identified as the points where the global or relative phase changes by 2π in a closed path around the point. The modulus and phase of A_x are also plotted. In the domains of argument defects, the modulus of A_x is constant and the phase is a spiral, in agreement with Eq. (14). In the domains of the director defects, $|A_x|$ has a characteristic radial structure that arises from the term $\cos(n\theta + \Delta\phi_0/2)$ in Eq. (15). The phase of A_x is a target pattern broken by a straight line where there is a phase jump of π. This jump is produced by the change of sign of the cosine in Eq. (15).

Figure 3 shows a scalar defect present in the A_+ component. It has been obtained at the same values of α and β as before, but $\gamma = 0.4$. At these parameter values, vectorial defects do not appear (as discussed later), so that the scalar ones are allowed to generate wave domains, as the one shown in Fig. 3. At the scalar defect core, where one of the component vanishes, the modulus of the other has a local maximum. Thus the object is circularly polarized and imposes some elliptic polarization to its neighborhood. The phase of A_+ is a spiral wave whose wavenumber can not be derived from the Hagan approach, since for scalar defects we have that $|A_+| \neq |A_-|$ (see Fig. 4) and no reduction to a single scalar CGL is possible. The wavenumber of the spiral wave is smaller than k_H. The phase of the nonvanishing component is almost constant. More precisely, this phase slowly changes with radial symmetry as one moves away from the center, so that the lines of constant phase form a target pattern. In a similar set of equations that include convective terms and a complex coupling, scalar defects have also been reported [27]. In that case, the phase of the nonvanishing field component presents a clearer target pattern. Phase target patterns in the scalar CGL equation are also found under suitable boundary conditions [28,29] or inhomogeneities [30]. The amplitudes and phases of the x and y linearly polarized components of the field around a scalar defect, also shown in Figs. 3 and 4, present spiral waves. Note that only phase waves, and not amplitude spiral waves, appear in the scalar CGL equation.

Figure 5 shows another view of scalar defects at two values of γ. The maximum in the modulus of the nonvanishing component, associated to the presence of the defect, is seen to grow with the value of γ, if $\gamma > 0$. This is a consequence of the coupling term in Eq. (3), which favors anticorrelation if $\gamma > 0$ (but positive correlation if $\gamma < 0$). Notice also that the size of the scalar defect-core increases with γ.

4 Defect dynamics for $|\gamma| < 1$

We first discuss all the theoretically possible processes of creation and annihilation of defects. These processes are illustrated in Fig. 6 where we plot in the horizontal axis the topological charge of the A_- component, and in the vertical axis the one of A_+. Open circles correspond to scalar defects, black circles to argument defects and gray circles to director defects, as in Fig. 2. The vectorial sum of arrows in the scheme implements the rule of topological charge conservation. The possible processes are: i) creation of a vector defect by the coalescence of two scalar defects (illustrated in Fig. 6(a) for an argument defect). This process is described in subsection 4.1. ii) Splitting of a vector defect in two scalar defects, which is in fact the inverse process, (see subsection 4.3). iii) Annihilation of a vector defect by collision with a scalar one. Fig. 6(b) represents the annihilation of an argument defect (the black dot) by collision with a scalar defect in the A_+ component (the open dot in the vertical axis), giving as a result a scalar defect in the A_- component (the open dot in the horizontal). Fig. 6(c) shows a similar annihilation process for a director defect (subsection 4.2).

Aranson and Pismen performed recently [17] an analytical study of the interactions between scalar defects at different field components, aiming at characterizing the stability properties of vector defects: if two scalar defects in different components attract each other, a vector defect will be formed in absence of other processes, whereas vector defects will be unstable if their components repel. A first result is that the interaction is long ranged, in contrast to the character of the interaction between defects in the same field. The approach in [17] is perturbative for small $|\gamma|$. The results depend on the value of κ, the parameter fixing the asymptotic value of the wavenumber. According to [17] there is a critical value $\kappa_c \simeq 0.52$ such that if $\kappa > \kappa_c$ two scalar defects in different components attract each other for $\gamma > 0$ [31]. For $\gamma < 0$, two scalar defects in different components attract each other if $\kappa < \kappa_c$. We find however numerically that for $\gamma < 0$ the vector defects have a short life time. The reason is that these defects generate a spiral with a small wavenumber k_H so that the group velocity at which perturbations are expelled away $v_g = 2(\alpha - \beta)k_H$ (see Appendix) is also small. It is then very likely that scalar defects in the neighborhood of the vector one (excluded from the analysis in [17]) approach its vector core and annihilate one of its components. In the following we focus our analysis of the dynamical properties of vector defects to the case $\gamma > 0$. Creation, annihilation and splitting of vector defects are described in the following three subsections. The relaxational case ($\alpha = \beta$) is discussed in subsection 4.4.

4.1 Creation of vector defects for $\gamma > 0$

If $\gamma = 0$ both components of the field behave independently and vector defects are thus not formed. For $\gamma \to 0$ the density of vector defects goes to zero for any value of α and β. But the behaviour for increasing γ depends on the values of α and β. It is useful to have in mind the different stability regions in α-β parameter space for the spirals in the scalar CGL equation, as described for example in [32]. Spirals simply can be absent (for $\kappa = 0$), or rather be stable, convectively unstable (the spirals remain in place and look stable because perturbations are effectively ejected away thanks to the group velocity on the spiral wave) or absolutely unstable. When the spirals are absolutely unstable defect turbulence develops. The extent of these regions is altered here by the coupling between the fields, given by the parameter γ.

If $\kappa \neq 0$, for a coupling $0 < \gamma < \gamma_d$ (where γ_d depends on α and β), vectorial defects are formed at short times starting from a random initial condition. Initially there is a high density of scalar defects. The density decreases as defects of opposite charges collide and annihilate in pairs in each component of the field. At this point, two scalar defects, one in A_+ and the other in A_-, may get close to each other, join and form a bound structure. This later stage is reached later as γ becomes smaller. Figure 7 shows the creation of a vectorial defect by displaying the sum of the field amplitudes, $|A_+|^2 + |A_-|^2$ ($\alpha = 0.2$, $\beta = 2$, so that $\kappa = 1.29 > \kappa_c \approx 0.52$, and $\gamma = 0.1$). For these values of α and β the scalar CGL (1) is in the region where the wavenumber k_H of the spirals is convectively unstable [32]. In the temporal sequence it can be seen that two dark dots, corresponding to the two scalar defects, one in each component of the field, get together and finally form the vector structure (the black dot). Immediately after the coalescence of both defects, the group velocity around the newly formed vector defect produces an exclusion region that precludes the approximation of other scalar defects. The region grows until the system arrives to a configuration similar to the one displayed in Fig. 1. The system has reached a frozen structure of domains separated by shock waves. The configuration in Fig. 1 is qualitatively similar to the ones encountered for the scalar CGL. Since very slow relaxation an other similarities with structural glasses have been pointed out in that case, the terms *glassy state* or *glass phase* are applied to it. We will use also these terms for the vectorial case (which is also seen to evolve in a very slow time scale). The peculiarity here is that, whereas in the scalar CGL the difference between the central defect and the defects at its domain border seems to arise from a spontaneous symmetry breaking, here all vector defects always expel from its domain the scalar ones, so that vector defects, if present, are always found at the center of wave domains.

The glassy configurations occur for relatively small γ. As γ is increased vec-

torial defects become unstable, leading to the melting of the glass phase. We have identified two mechanisms by which this process occurs, to which the next two subsections are devoted: (i) domain instability and (ii) core instability. In the case of domain instability the domain around a vector defect becomes unstable and develops inhomogeneities. These irregularities lead to paths that permit the approach of a scalar defect that finally collides with the core and annihilates one of the components of the vector defect. In the core instability case the vector defect simply splits in two scalar defects. This process is described in Ref. [12] for the real coefficient case, where a greater symmetry between director and argument defects seems to be present and both kind of defects become unstable for the same value of γ. As we will see in Sect. 4.3, this is not the case for complex coefficients.

Finally, in the region of parameter space α-β where spirals are absolutely unstable [32] for the scalar CGL equation, no vectorial defects are formed. In this case we have what is called in the scalar case defect turbulence. Increasing γ does not change the qualitative behavior of each component, although anticorrelation between the modulus of both components increases.

4.2 Domain instability

By 'domain instability' we denote the situation in which the wave domain around a vector defect becomes unstable, begins to fluctuate, and develops inhomogeneities. Shortly afterwards one of the two charges forming a vector defect is annihilated by an external scalar defect. As a result a free scalar defect is left in the other component of the field. The region of parameter space α-β where this process is observed corresponds approximately to the region where for the scalar CGL equation the phase spirals are convectively unstable [32]. As γ is increased from zero the stability of the spirals is modified: At a given value of γ, the group velocity is not strong enough to overwhelm the growth of the perturbations, the spirals becoming absolutely unstable. At this point the domains around the vectorial defects are uneffective as exclusion zones, so that scalar defects previously confined to the domain border can approach the vectorial defect core. Although this picture is valid for both kinds of vectorial defects, director defects survive for larger γ than argument ones. For the parameter values of Fig. 1, argument defects become unstable at $\gamma \simeq 0.3$ (see Fig. 8), while director defects remain stable up to $\gamma \simeq 0.35$ (see Fig. 9). For larger γ only scalar defects are found numerically.

The different stability range of argument and director defects can be understood through a linear stability analysis of the vector spirals focusing in its plane-wave structure far from the core. This analysis is performed in the Appendix. The main point to be recognized is the difference between the phase

structure between argument and director vector defects. In Figs. 10 (a) and (b) we show constant phase curves of both components for an argument defect and a director defect. The wave vectors of the components A_+ and A_- in a point $\mathbf{x}$, $\mathbf{k}_+(\mathbf{x})$ and $\mathbf{k}_-(\mathbf{x})$ are perpendicular to the constant-phase curves. As discussed before, $k_+ = k_- = k_H$, where k_H is the wave number of a scalar spiral. For the argument defects the difference of wave vectors $\mathbf{k_R} = \mathbf{k}_+ - \mathbf{k}_-$ vanishes at any point of the plane while for the director defects $\mathbf{k_R} \neq 0$. Far from the defect core, $\mathbf{k_R}$ decreases for the director defect, however it remains different from 0 within the exclusion island surrounding the defect.

The linear stability analysis of the wave in the two cases turns out to be different. It is shown in the Appendix that for argument defects, a wave with $k_+ = k_- = k_H$ becomes unstable if $k_H > K_p$, where $K_p(\alpha, \beta, \gamma)$ is given in Eq. (25), while in the case of director defects this happens if $k_H > K_s$, where $K_s(\alpha, \beta, \gamma)$ is given in Eq. (22).

In figures 11 (a) and (b) we plot stability diagrams in the α-β plane, with the line $1 + \alpha\beta = 0$ as a reference. In fig. 11 (a) we show the curves $K_p = k_H$ and $K_s = k_H$ for $\gamma = 0.3$. To the right of the curves, plane waves with $k = k_H$ are unstable. In fig. 11 (b) we plot the curve $K_p = k_H$ for different values of γ ($\gamma = 0, 0.3, 0.6, 0.9, 0.99$). We can see that the curve moves left and upwards as γ is increased; the same happens with the curve $K_s = k_H$. Let us consider a point (α_0, β_0) such that plane waves with $k = k_H$ are stable for $\gamma = 0$. As γ is increased the curve $K_p = k_H$ crosses the point turning the vectorial waves with $\mathbf{k_R} = 0$ unstable, this destabilizes the domains of the argument defects. If γ is further increased, then the curve $K_s = k_H$ crosses the point (α_0, β_0) and waves with $\mathbf{k_R} \neq 0$ become unstable, destabilizing the domains of the director defects. It should be said that the kind of stability analysis performed in the Appendix considers extended perturbations. Since spiral waves have a group velocity, it may happens that these instabilities are of convective type, that is, localized perturbations do not destroy the spiral wave but they are advected away from the defect core of the spiral with the group velocity [32]. Thus, we can still find stably-looking spirals although the corresponding plane waves far from the core are unstable. The calculation of the limit of *absolute instability* to localized perturbations is quite involved, but the result for the convective instability suggests that corotating spirals become absolutely unstable before counterrotating ones. We believe that the analysis presented here is an indication of the kind of instabilities that can affect the vectorial spirals and the order in which they appear as the coupling parameter γ is increased.

4.3 Core instability

A core instability of a vector defect occurs when it splits in two scalar defects. This process is roughly present in the region of parameter space α-β where the spirals are stable in the scalar case. The splitting of a director defect is shown in Fig. 12 for $\kappa = 0.54$ and $\gamma = 0.95$. The size of the vectorial defect-core is much narrower than the size of the core of the two scalar defects that remain at the end of the process. This is a consequence of two facts mentioned before, namely that the size of the vectorial defects does not depend on γ, whereas the size of scalar defects increases. Also in this case argument defects become unstable for smaller γ than director defects. For example, for the parameter values of Fig. 12 argument defects already split for $\gamma = 0.75$.

After the splitting, both scalar defects may form a bound pair that resembles a rotating molecule [17]. In Fig. 13 a temporal sequence is plotted that shows a pair of scalar defects that rotate one around the other. For the particular values of the figure, however, the distance between the scalar defects increases and the angular velocity decreases, thus the molecule finally unbinds. Stable molecules, however, are found for other parameter values as reported in [17].

4.4 The relaxational case: $\alpha = \beta$

Qualitative features distinguish the case $\alpha = \beta$ ($\kappa = 0$) from the other cases: First, no spiral wave is formed around vector defects (since, as stated before, $k_H = 0$ if $\kappa = 0$). Second, the group velocity with which linear perturbations are expelled away from the neighborhood of a vector defect is zero (the group velocity is $v_g = 2(\alpha - \beta)k_H$, as shown in the Appendix). Thus, perturbations and other defects are rather free to come arbitrarily close to vector defects if $\kappa = 0$ and we expect them to be frequently annihilated by processes such as the ones shown in Fig. 6(b) or (c).

Starting from random initial conditions we do not find numerically the formation of vectorial defects in Eq. (3) for $\alpha = \beta$ and $\gamma > 0$. In Fig. 14, the quantities $|A_+|^2$ and $|A_-|^2$ are plotted for $\alpha = \beta = 0$ and $\gamma = 0.1$. It can be seen that there is no superposition of two defects in the same point. Starting with an initial condition with a slightly perturbed vector defect, it spontaneously splits into two scalar defects for any positive γ, as can be seen in Fig. 15 for $\gamma = 0.2$. This behavior is in agreement with the predictions of [17].

More in general, approaching the line $\alpha = \beta$, we observe numerically that director and argument defects of initial configurations such as the one in Fig. 1 split spontaneously, even for very small values of γ, again in agreement with [17].

5 The gas phase

For γ high enough, the vectorial defects always disappear following one of the two mechanisms described above. The system then presents a faster disordered dynamics compared with the *glassy* phase with vector defects. It is a kind of *gas-like* phase, dominated by the scalar defects, which are conserved in number during very long times. The scalar defects move faster than in the glassy phase, in a way reminiscent of atoms in a gas, from which we borrow the name. Furthermore, the spiral wavelength around scalar defects increases with γ, so that well-developed spirals do not fit in the domains for γ close to one. Domains are thus less effective as exclusion zones and defects even more mobile.

To distinguish the presence of these two different phases we can use the joint probability distribution of the modulus of the field components: $p(|A_+|, |A_-|)$. Figure 16 shows a grey scale plot of $p(|A_+|, |A_-|)$ for $\gamma = 0.1$ (glassy phase) and $\gamma = 0.95$ (gas phase); in both cases $\alpha = 0.2$ and $\beta = 2$. The plot is obtained taking the values of $(|A_+|,|A_-|)$ at different space-time points. For $\gamma = 0.1$ there is a broad maximum around $|A_+| \simeq |A_-| \simeq 0.85$ with deviations from these values being rather uncorrelated, except for the points lying in the line $|A_+| = |A_-|$. This line shows that the absolute values of both components take simultaneously the same value between 0 and 1, situation identifying the core of vector defects. For $\gamma = 0.95$ the line $|A_+| = |A_-|$ has disappeared due to the absence of vector defects. Instead, the probability distribution approaches the curve given by $|A_+|^2 + |A_-|^2 = 1$, which indicates anticorrelation between $|A_+|$ and $|A_-|$. This anticorrelation is the fingerprint of the dominance of the scalar defects (See Figs. 4 and 5). Similar qualitative behaviour is observed for other values of α and β (given that $\kappa > \kappa_c$) as γ is increased.

The behavior in the glass and in the gas phase can be interpreted in terms of synchronization and generalized synchronization, respectively, of spatiotemporally chaotic configurations of the two field components [18,14]. In this context, another interesting quantity that gives information about the transition from the glassy to the gas phase is the mutual information between field components, that can be computed from the individual and joint probability densities. In general, for two random discrete variables X and Y the mutual information

$$I(X,Y) = -\sum_{x,y} p(x,y) \ln \frac{p(x)p(y)}{p(x,y)}$$

gives a measure of the statistical dependence between both variables, the mutual information being 0 if and only if X and Y are independent [33]. Numerical results presented in [14] show that there is a minimum of $I(|A_+|, |A_-|)$ ($\gamma \simeq 0.3$ at $\alpha = 0.2$ and $\beta = 2$), where the variables have been adequately discretized, and that this value of γ can be interpreted as the transition point

from the glassy to the gas phase. See [14] and [15] for more details about the vortex unbinding transition between the glassy and the gas-like phases.

6 Dynamics for $\gamma > 1$

For $\gamma > 1$, as discussed in Sec. 2, linearly polarized states become unstable with respect to circularly polarized states. In this case the system segregates in two phases, one right circularly polarized and the other left circularly polarized. Figure 17 is an example of a configuration that started from a random initial condition ($\gamma = 1.1$, $\alpha = 0.2$, $\beta = 2$). Phase separation is clearly observed. As the system evolves, the length of the interface walls is reduced, in a domain-coarsening process. Despite the tendency of the concave domains to shrink, some defects remain at long times. Vector point defects are no longer topologically allowed since the stable uniform states are such that the vanishing of one of the two polarizations in large areas, not just at points, is favored. However we still have scalar point defects that are now lying on the domains of one circular polarization, and are points at which the corresponding field amplitude goes to zero. Only one topological charge is defined, the associated to the component which vanishes just at one point. They are of the type described in [11,12] as having a 'repolarized core' structure: In domains filled with one of the polarizations, say +, a defect is a place at which $|A_+|$ goes to zero, thus producing a phase singularity (seen in Fig. 17) associated to a topological charge $n_+ = \pm 1$; in response to this behavior the component which does not carry the topological charge takes nonzero values in the defect-core region. Other structures for the core are in principle possible, as for example a 'punched core' structure in which the component that does not carry the charge remains vanishing in the defect-core region. As discussed in [11,12], topological arguments imply that only the 'repolarized core' should be observed for γ slightly above 1, and this is indeed what Fig. 17 shows. The differences in the sizes of the defect cores seen in Fig. 17 disappear at longer times.

We stress that the topological defects in Fig. 17 are different from the localized structures found in other systems with coexistence of two equivalent homogeneous states, such as the Swift-Hohenberg equation in adequate parameter ranges or the parametrically forced CGL equation. In these systems the oscillating tails of the fronts connecting the two equivalent homogeneous solutions are responsible for maintaining the existence of localized structures against the tendency of the domains to shrink [34]. These localized structures are not topological defects. Here, on the contrary, it is the topological character of the objects what prevents them to disappear after shrinking to a point: defects can only disappear by combination with others of opposite charge.

7 Conclusions

We have numerically explored the conditions for the existence and stability of the different kinds of defects in the twodimensional VCGL equation: vector defects of argument or director type, and scalar defects. Dynamic phenomena associated with their creation and annihilation processes have been described. In particular, we have identified two mechanisms that lead to the destruction of the vector defects as the coupling parameter between field components is increased: domain instability and core instability. One or the other takes place depending on parameters α and β. For the domain instabilities of vector defects we have obtained analytic understanding in terms of the convective instability of the emitted spiral wave. For the core instability at a relatively large threshold value of γ there is no available theory so far.

Our numerical results have been compared with the useful analytical studies by Aranson and Pismen [17]. They studied core instabilities as a function of α and β for small γ. Their results explain our result that in the relaxational limit ($\alpha = \beta$) there are no vectorial defects for $\gamma > 0$. They also explain the existence of vector defects far from the relaxational limit and for small γ. Our main interest, however, was on what happens far from the relaxational limit as function of γ. In this regime we have found threshold values of γ for the domain and core instabilities mentioned before. These instabilities are not accessible to the perturbative theoretical discussion of Aranson and Pismen and there is need of further analytical studies.

Finally, the dominance of different types of defects at different parameter values leads to the identification of different dynamical regimes, such as the glassy and the gas phase.

Acknowledgments

Financial support from MCyT (Spain), project CONOCE BMF2000-1108, is acknowledged. M. H. acknowledges financial support of Fundación Antorchas, Argentina, and of the National Council for Scientific and Technical Research (CONICET) from Argentina.

Appendix

We analyze in this Appendix the stability of the wave emitted by vector defects. Far from the defect core we can approximate the spiral waves by plane

waves. The stability of plane waves with wave number k_H will give us information about the stability of the spirals. The stability analysis presented here is an extension to two dimensions of the analysis made in one dimension in [13] and it is valid for $|\gamma| < 1$. The effect of a perturbation on the plane wave solution (4) can be written as

$$A_\pm = (Q + a_\pm)e^{-i(\mathbf{k}_\pm \cdot \mathbf{r} - \omega_\pm t + \phi_{0\pm})} \tag{16}$$

where $|\mathbf{k}_+| = |\mathbf{k}_-| = k_H$ for a vector defect. Q and ω are given by Eq. (7), and $a_\pm$ are the complex perturbations. Using the variables

$$\begin{Bmatrix} s \\ s_I \\ r \\ r_I \end{Bmatrix} = \begin{Bmatrix} \Re(a_+ + a_-) \\ \Im(a_+ + a_-) \\ \Re(a_+ - a_-) \\ \Im(a_+ - a_-) \end{Bmatrix}, \tag{17}$$

where $\Re$ and $\Im$ mean real and imaginary part, respectively, we obtain linearized equations for s, s_I, r and r_I. Instabilities appear first in the phase modes. They are identified as the linear combinations of the variables that in the space-homogeneous case lead to zero eigenvalues. They are $\theta = -\beta s + s_I$ and $\psi = -\beta r + r_I$. Performing the change of variables $(s, r, s_I, r_I) \to (s, r, \theta, \psi)$, and eliminating adiabatically the rapidly decaying amplitude variables s and r in terms of the phases, we get the following phase equations:

$$\begin{aligned}
\partial_t\theta =& (\alpha - \beta)\mathbf{k_S} \cdot \nabla\theta + (1 + \alpha\beta)\nabla^2\theta - \frac{(1+\beta^2)}{2(1-k^2)}\left[(\mathbf{k_S} \cdot \nabla)^2\theta + \frac{1+\gamma}{1-\gamma}(\mathbf{k_R} \cdot \nabla)^2\theta\right] \\
&+(\alpha - \beta)\mathbf{k_R} \cdot \nabla\psi - \frac{(1+\beta^2)}{(1-k^2)(1-\gamma)}(\mathbf{k_S} \cdot \nabla)(\mathbf{k_R} \cdot \nabla)\psi, \\
\partial_t\psi =& (\alpha - \beta)\mathbf{k_S} \cdot \nabla\psi + (1 + \alpha\beta)\nabla^2\psi - \frac{(1+\beta^2)(1+\gamma)}{2(1-k^2)(1-\gamma)}\left[(\mathbf{k_S} \cdot \nabla)^2\psi + \frac{1-\gamma}{1+\gamma}(\mathbf{k_R} \cdot \nabla)^2\psi\right] \\
&+(\alpha - \beta)\mathbf{k_R} \cdot \nabla\theta - \frac{(1+\beta^2)}{(1-k^2)(1-\gamma)}(\mathbf{k_S} \cdot \nabla)(\mathbf{k_R} \cdot \nabla)\theta,
\end{aligned} \tag{18}$$

where $\mathbf{k_S} = \mathbf{k}_+ + \mathbf{k}_-$ and $\mathbf{k_R} = \mathbf{k}_+ - \mathbf{k}_-$.

As explained in Sect. 4.2, $\mathbf{k_R} = 0$ in the domain surrounding argument defects, but $\mathbf{k_R} \neq 0$, although small, for the domain around director defects. In both cases one can approximate $|\mathbf{k_S}| \approx 2k_H$. For small $\mathbf{k_R}$, the dominant first-order derivative terms in (18) indicate that small perturbations on the waves travel at a group velocity $v_g = 2(\alpha - \beta)k_H$.

We consider perturbations of small wave vector $\mathbf{q}$. The eigenvalues of the linear system (18) are,

$$\frac{\lambda_\pm}{q^2} = -1 - \alpha\beta + \frac{(1+\beta^2)}{2Q^2(1-\gamma^2)}\left[(\mathbf{k_R}\cdot\hat{\mathbf{q}})^2 + (\mathbf{k_S}\cdot\hat{\mathbf{q}})^2\right] \pm \frac{\sqrt{S}}{2q} \qquad (19)$$

where $q = |\mathbf{q}|$, $\hat{\mathbf{q}} = \mathbf{q}/q$ is the direction of the perturbation vector, and $S = aq^2 + ibq - c$, with,

$$\begin{aligned} a &= \frac{(1+\beta^2)^2}{Q^4(1-\gamma^2)^2}\left\{\gamma^2\left[(\mathbf{k_R}\cdot\hat{\mathbf{q}})^2 - (\mathbf{k_S}\cdot\hat{\mathbf{q}})^2\right]^2 + 4(\mathbf{k_R}\cdot\hat{\mathbf{q}})^2(\mathbf{k_S}\cdot\hat{\mathbf{q}})^2\right\} \\ b &= 8(\alpha-\beta)\frac{(1+\beta^2)}{Q^2(1-\gamma^2)}(\mathbf{k_R}\cdot\hat{\mathbf{q}})^2\mathbf{k_S}\cdot\hat{\mathbf{q}} \\ c &= 4(\alpha-\beta)^2(\mathbf{k_R}\cdot\hat{\mathbf{q}})^2 \quad . \end{aligned} \qquad (20)$$

If $\mathbf{k_R} \neq 0$, as is the case for director defects, we can approximate $\sqrt{S} = i\sqrt{c}(1 - \frac{ib}{2c}q) + O(q^2)$. The real part of the two eigenvalues are,

$$\frac{\Re(\lambda_\pm)}{q^2} = -1 - \alpha\beta + \frac{2(1+\beta^2)}{Q^2(1-\gamma^2)}k^2\cos^2\chi_\pm + O(q), \qquad (21)$$

where $\chi_\pm$ are the angles between the perturbation wave vector $\mathbf{q}$ and the wave vectors $\mathbf{k}_+$ and $\mathbf{k}_-$. Since $|\mathbf{k_R}|$ is finite the instability may arise for perturbation wavenumber q *smaller* than $|\mathbf{k_R}|$. In this case, considering the most dangerous longitudinal perturbations, i.e. when $\chi_+ = 0$ or $\chi_- = 0$, we obtain a critical wave number K_s such that if $k > K_s$ the plane waves become Eckhaus unstable. Taking $\Re(\lambda_\pm) = 0$ in (21) we get,

$$K_s^2 = \frac{(1+\alpha\beta)(1-\gamma)}{(1+\alpha\beta)(1-\gamma) + 2(1+\beta^2)}. \qquad (22)$$

The equations for $\partial_t\theta$ and $\partial_t\psi$ (18) are coupled, and the eigenvector corresponding to the unstable eigenvalue mixes both variables. This means that the sum and the difference of the field perturbations a_+ and a_-, become unstable simultaneously in this case.

If $\mathbf{k_R} = 0$, as appropriate around argument defects, we have that $\mathbf{k}_+ = \mathbf{k}_-$, and $\chi_+ = \chi_- = \chi$, and

$$S = \left(\frac{(1+\beta)\gamma kq\cos\chi}{Q^2(1-\gamma^2)}\right)^2 \quad . \qquad (23)$$

We obtain for the real parts of the eigenvalues,

$$\frac{\Re(\lambda_\pm)}{q^2} = -1 - \alpha\beta + \frac{2(1+\beta^2)(1\pm\gamma)}{Q^2(1-\gamma^2)}k^2\cos^2\chi + O(q). \tag{24}$$

We consider again longitudinal perturbations corresponding to $\chi = 0$. Taking the marginal stability condition in (24) for the most dangerous eigenvalue, $\Re(\lambda_+) = 0$, we see that in this case plane waves become unstable for $k > K_p$, where K_p is given by,

$$K_p^2 = \frac{(1+\alpha\beta)(1-\gamma)}{(1+\alpha\beta)(1-\gamma) + 2(1+\beta^2)(1+|\gamma|)}. \tag{25}$$

For $\mathbf{k_R} = 0$, the equations (18) for $\partial_t\theta$ and $\partial_t\psi$ are decoupled. The most restrictive eigenvalue, λ_+, is associated with the variable ψ, which is related to the difference of the field perturbations. When ψ becomes unstable, the difference $a_+ - a_-$ grows; in optical language this is called a polarization instability.

References

[1] H. Riecke, in *Pattern formation in continuous and coupled systems*, ed. by M. Golubitsky, D. Luss and S. H. Strogatz (Springer, New York, 1999); L. M. Pismen, *Vortices in nonlinear fields*, (Oxford Univ. Press, New York, 1999).

[2] F.T. Arecchi *et al.* Phys. Rev. Lett. **67**, 3751 (1991); K. Staliunas, G. Slekys and C. O. Weiss, Phys. Rev. Lett. **79**, 2658 (1997); C. O. Weiss *et al.* Appl. Phys. **B 68**, 151 (1999); N. N. Rosanov, in *Progress in Optics. Vol. 35*, Ed. by E. Wolf (North-Holland, Amsterdam, 1996); M. Brambilla *et al.* Phys. Rev. Lett. **79**, 2042 (1997); D. Michaelis, U. Peschel and F. Lederer, Phys. Rev. **A 56**, R3366 (1997); M. Tlidi, P. Mandel and R. Lefever, Phys. Rev. Lett. **73**, 640 (1994); W. Firth and A.J. Scroggie, Phys. Rev. Lett. **76**, 1623 (1996); C. Etrich, U. Peschel, and F. Lederer, Phys. Rev. Lett. **79**, 2454 (1997); K. Staliunas and J.V. Sánchez-Morcillo, Phys. Rev. **A 57**, 1454 (1998); G.L. Oppo, A.J. Scroggie, and W.J. Firth, J. Opt. B: Quant. Semiclass. Opt. **1**, 133 (1999).

[3] R. Bhandari, Phys. Rep **281**, 1 (1997).

[4] M. Santagiustina, E. Hernández-García, M. San Miguel, A.J. Scroggie, G.-L. Oppo, *Polarisation Patterns and Vectorial Defects in Type II Optical Parametric Oscillators*, Phys. Rev. E, to appear (2002).

[5] R. Gallego, M. San Miguel and R. Toral, Phys. Rev. E **61**, 2241 (2000).

[6] M. C. Cross and P. C. Hohenberg, Rev. Mod. Phys **65**, 851 (1993).

[7] T. Bohr, M. Jensen, G. Paladin, and A. Vulpiani, *Dynamical Systems Approach to Turbulence* (Cambridge Univ. Press, Cambridge, 1998).

[8] I. S. Aranson, L. Kramer, Rev. Mod. Phys. **74**, 99 (2002).

[9] L. Gil, Phys. Rev. Lett. **70**, 162 (1993).

[10] L. Gil, Int. J. Bif. Chaos **3**, 573 (1993).

[11] L. M. Pismen, Phys. Rev. Lett. **72**, 2557, (1994).

[12] L. M. Pismen, Physica **D 73**, 244 (1994).

[13] M. San Miguel, Phys. Rev. Lett. **75**, 425 (1995).

[14] E. Hernández-García, M. Hoyuelos, P. Colet, M. San Miguel and R. Montagne, Int. J. Bif. and Chaos **9**, 2257 (1999).

[15] M. Hoyuelos, E. Hernández-García, P. Colet and M. San Miguel, Comp. Phys. Comm. **121-122**, 414 (1999).

[16] E. Hernández-García, M. Hoyuelos, P. Colet, M. San Miguel, Phys. Rev. Lett. **85**, 744 (2000).

[17] I. S. Aranson and L. M. Pismen, Phys. Rev. Lett. **84**, 634 (2000).

[18] A. Amengual, E. Hernández-García, R. Montagne and M. San Miguel, Phys. Rev. Lett. **78**, 4379 (1997).

[19] R. Montagne and E. Hernández-García, Phys. Lett. **A 273**, 239 (2000).

[20] R. Montagne, E. Hernández-García, and M. San Miguel, Physica **D 96**, 47 (1996).

[21] M. San Miguel, R. Montagne, A. Amengual, and E. Hernández-García, in *Instabilities and non-equilibrium structutures V*, edited by E. Tirapegui and W. Zeller (Kluwer, Dordrecht, 1996).

[22] A.J. Leggett, Rev. Mod. Phys. **73**, 307 (2001).

[23] J. Yang, Y. Tan, Phys. Rev. Lett. **85**, 3624 (2000), and references therein.

[24] The integration algorithm is the one presented in [15], which is a generalization to the vector case of the pseudospectral in space and second-order in time algorithm for the CGL equation of [26]. We discretize with a 128×128 square lattice a domain of 64×64 space units with periodic boundary conditions. Animations of the different dynamic phenomena can be downloaded from `http://www.imedea.uib.es/PhysDept/Nonlinear/research_topics/Vcgl2/`.

[25] P. S. Hagan, SIAM J. Appl. Math. **42**, 762 (1982).

[26] R. Montagne, E. Hernández-García, A. Amengual, and M. San Miguel, Phys. Rev. **E 56**, 151 (1997).

[27] J. Lega, C. R. Acad. Sci. Paris **309**(II), 1401 (1989).

[28] V. M. Eguíluz, E. Hernández-García and O. Piro, Int. J. of Bif. and Chaos **9**, 2209 (1999).

[29] V. M. Eguiluz, E. Hernández-García and O. Piro, Phys. Rev. **E 64**, 036205 (2001).

[30] M. Hendrey, K. Nam, P. Guzdar, and E. Ott, Phys. Rev. **E 62**, 7627 (2000).

[31] Earlier theoretical analysis [11] left open the possibility for the existence of vector defects below a critical value of the coupling, $\gamma_c \simeq 0.492$, for $\alpha = \beta = 0$, but the more recent work [17] rules out this possibility, or equivalently $\gamma_c = 0$.

[32] I. S. Aranson, L. Aranson, L. Kramer and A. Weber, Phys. Rev. A **46**, R2992 (1992); I. S. Aranson, L. Kramer and A. Weber, in *Instabilities and Nonequilibrium Strutctures IV*, pag. 259, edited by E. Tirapegui and W. Zeller (Kluwer Academic Publishers, 1993).

[33] R. J. McEliece, *The theory of Information and Coding: a Mathematical Framework for Communication*, Encyclopedia of Mathematics and its Applications, Vol. III (Addison-Wesley, New York, 1977).

[34] P. Coullet, C. Elphick, and D. Repaux, Phys. Rev. Lett. **58**, 431 (1987); D. Gomila, P. Colet, G.-L. Oppo, M. San Miguel, Phys. Rev. Lett. **87**, 194101 (2001).

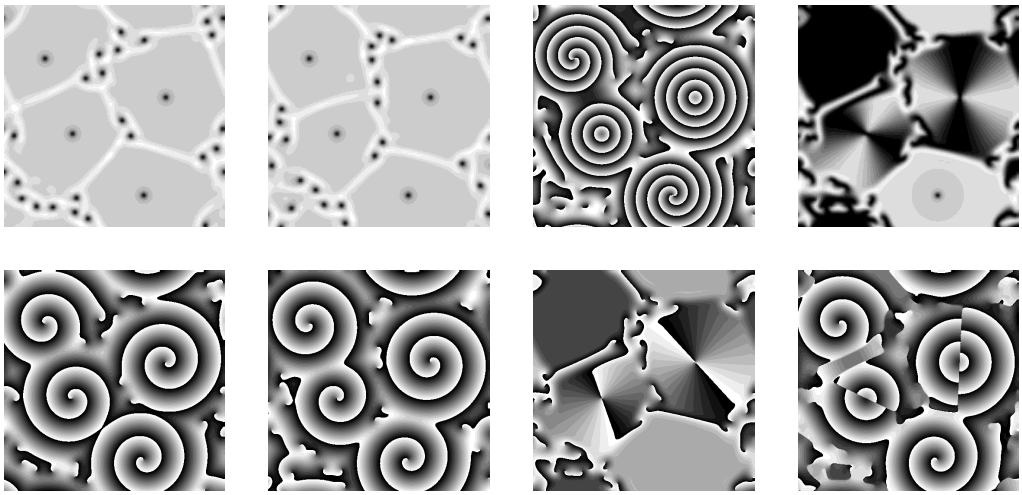

Fig. 1. Vectorial defects for $\gamma = 0.1$, $\alpha = 0.2$ and $\beta = 2$ ($\kappa = 1.29$). From left to right, top row: $|A_+|^2$, $|A_-|^2$, global phase ϕ_g, and $|A_x|^2$. Bottom row: ϕ_+, ϕ_-, relative phase ϕ_r, and phase of A_x. Here and in the following figures, the values are coded in gray scale. In the images displaying amplitude values, black means zero amplitude, and thus the presence of a defect.

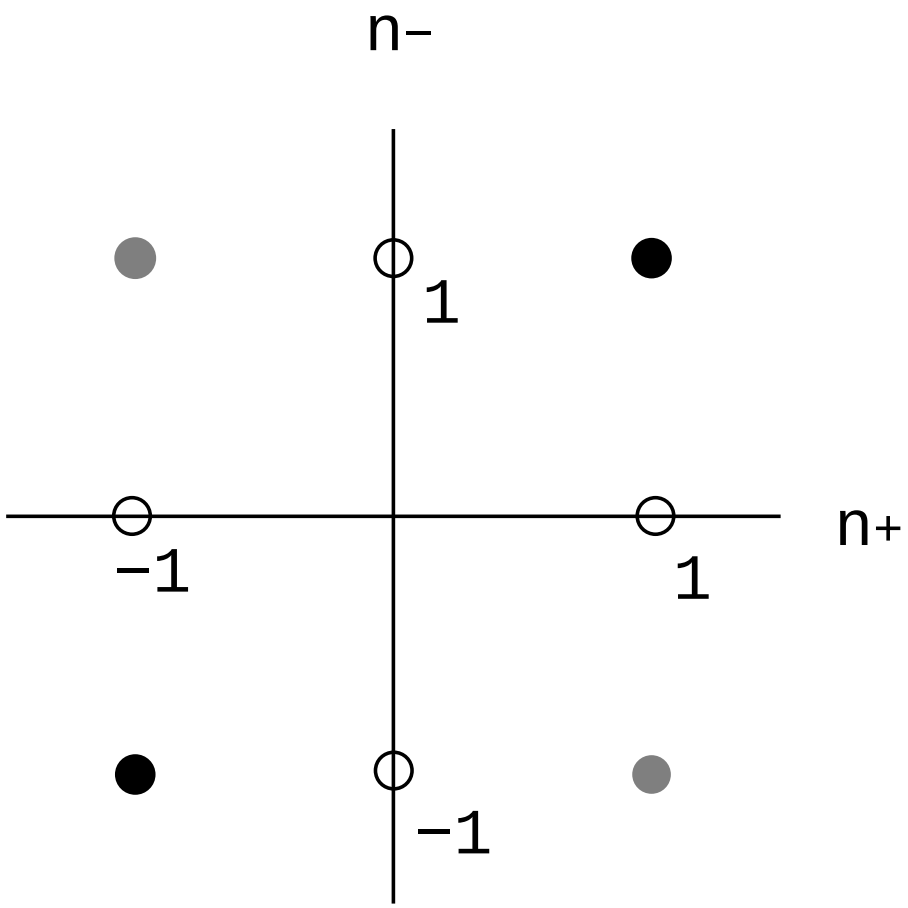

Fig. 2. Scheme showing the possible defects according to different combination of the charges n_+ and n_-. White dots correspond to scalar defects, black dots to vectorial argument defects, and gray dots to vectorial director defects.

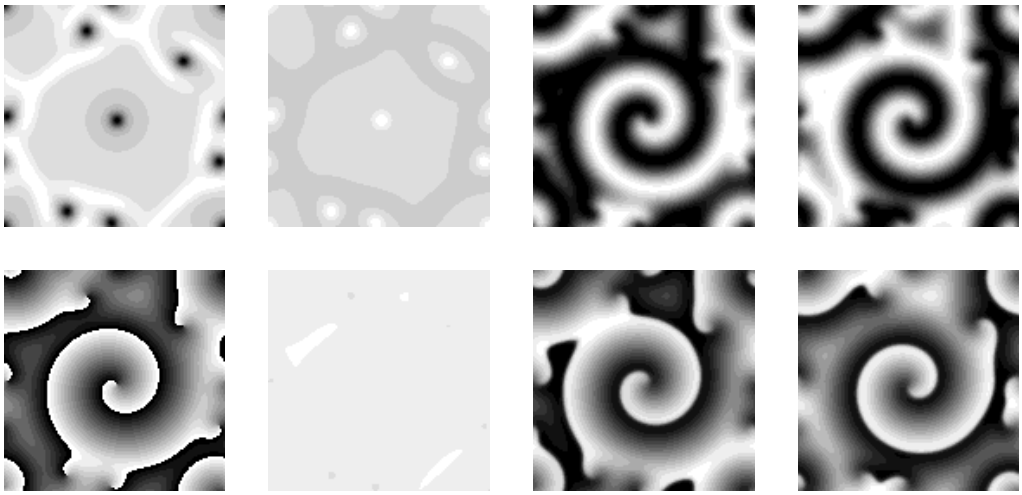

Fig. 3. Different views of a scalar defect for $\gamma = 0.4$, $\alpha = 0.2$ and $\beta = 2$ ($\kappa = 1.29$), present in the A_+ component. From left to right, top row: $|A_+|^2$, $|A_-|^2$, $|A_x|^2$ and $|A_y|^2$; bottom row: ϕ_+, ϕ_-, and phases of A_x and A_y,

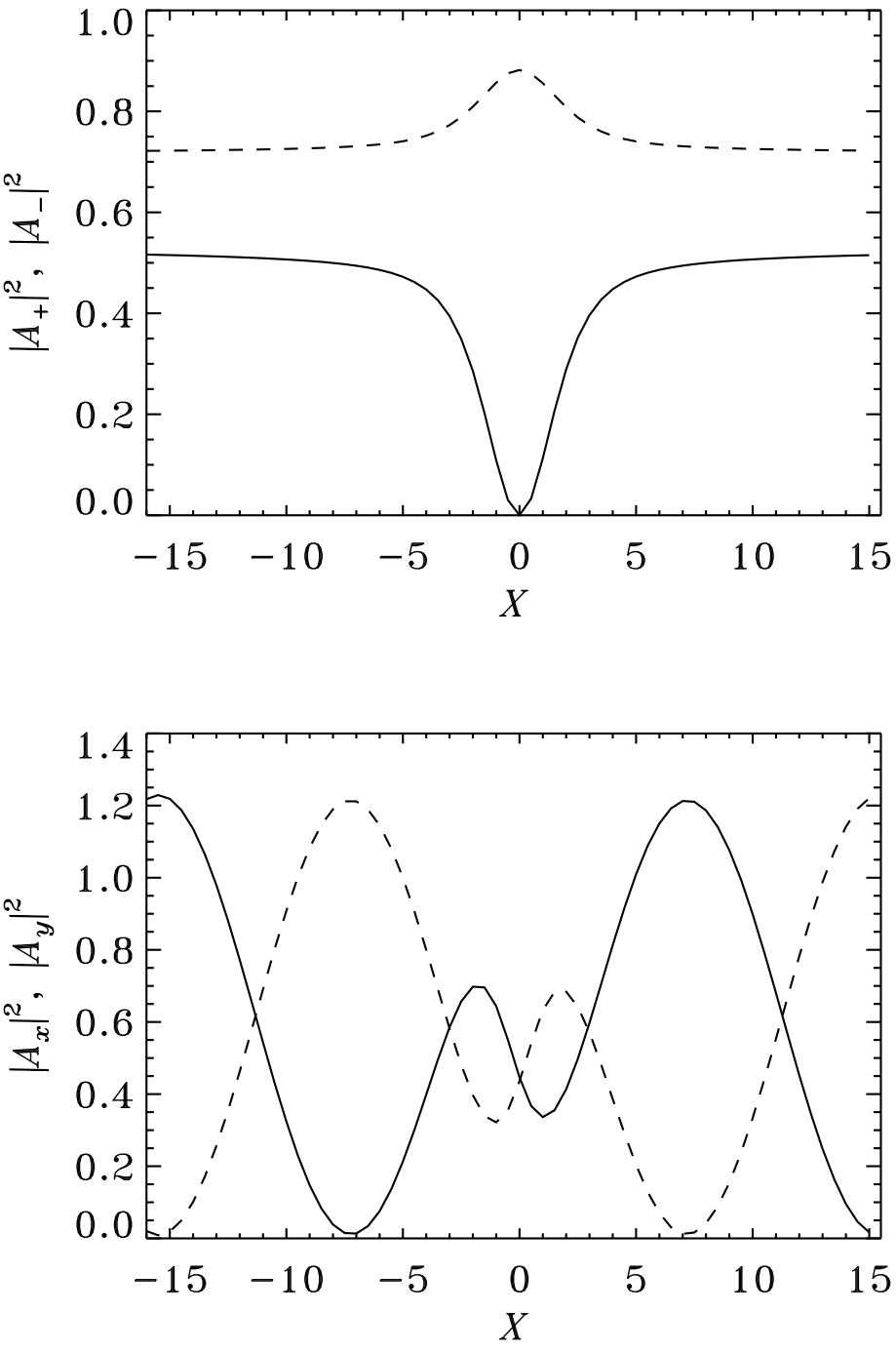

Fig. 4. Cross sections of the intensities of a scalar defect (same parameters as in Fig. 3). The top figure shows the defect in the + component (solid line), and associated maximum in $|A_-|^2$ (dashed line). Bottom figure: the spiral waves in the x and y amplitudes are out of phase (compare with Fig. 3).

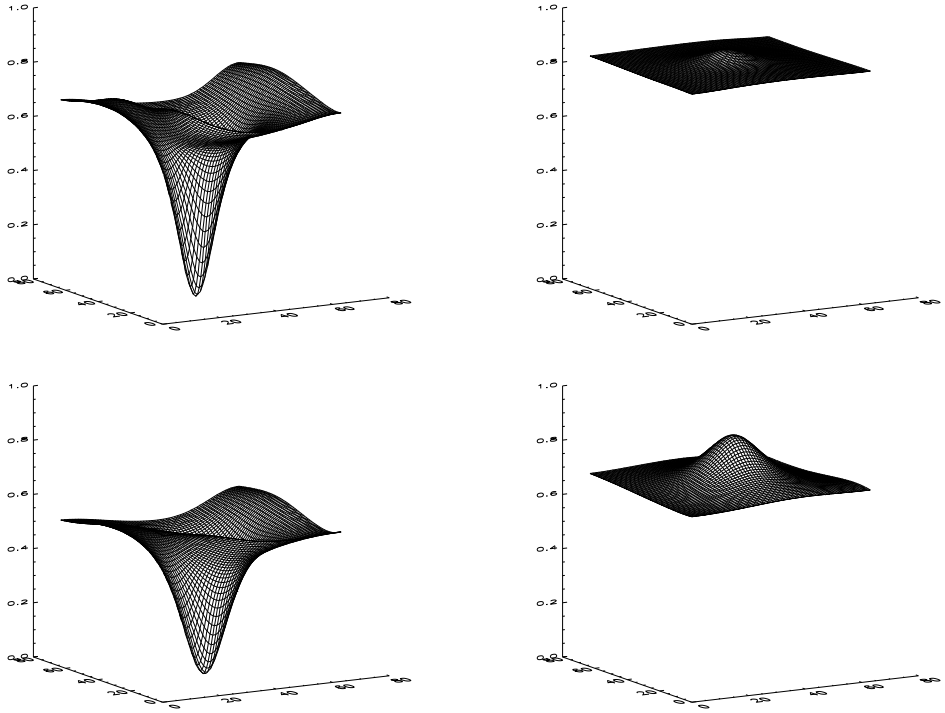

Fig. 5. Scalar defects at different values of γ, as a function of the two spatial coordinates. First row: $|A_+|^2$ (left) and $|A_-|^2$ (right) at $\gamma = 0.1$. Second row: Idem for $\gamma = 0.4$. In both cases $\kappa = 1.29$, and the singular component is A_+.

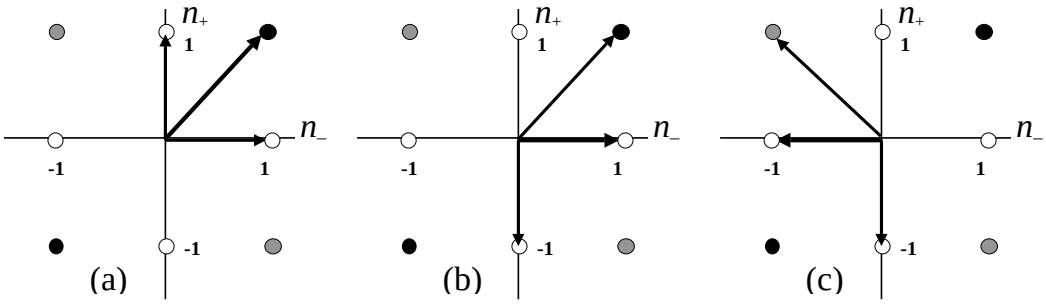

Fig. 6. Scheme showing some possible creation and destruction processes of defects in the n_+-n_- plane. See text for details. (a) Creation of an argument defect, (b) annihilation of an argument defect due to the collision with a scalar defect with charge $n_- = -1$, (c) annihilation of a director defect.

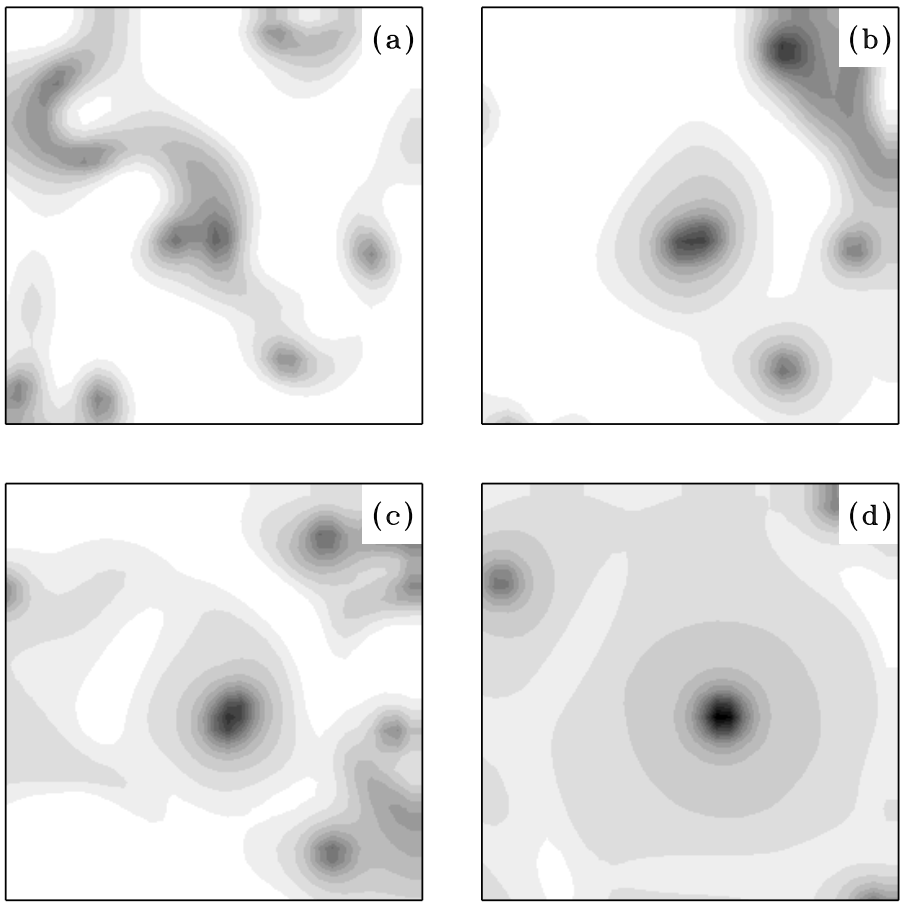

Fig. 7. Temporal sequence of $|A_+|^2 + |A_-|^2$ showing the formation of a vectorial defect at short times for $\gamma = 0.1$ and $\kappa = 1.29$. (a) $t = 15$, (b) $t = 30$, (c) $t = 45$, and (d) $t = 150$.

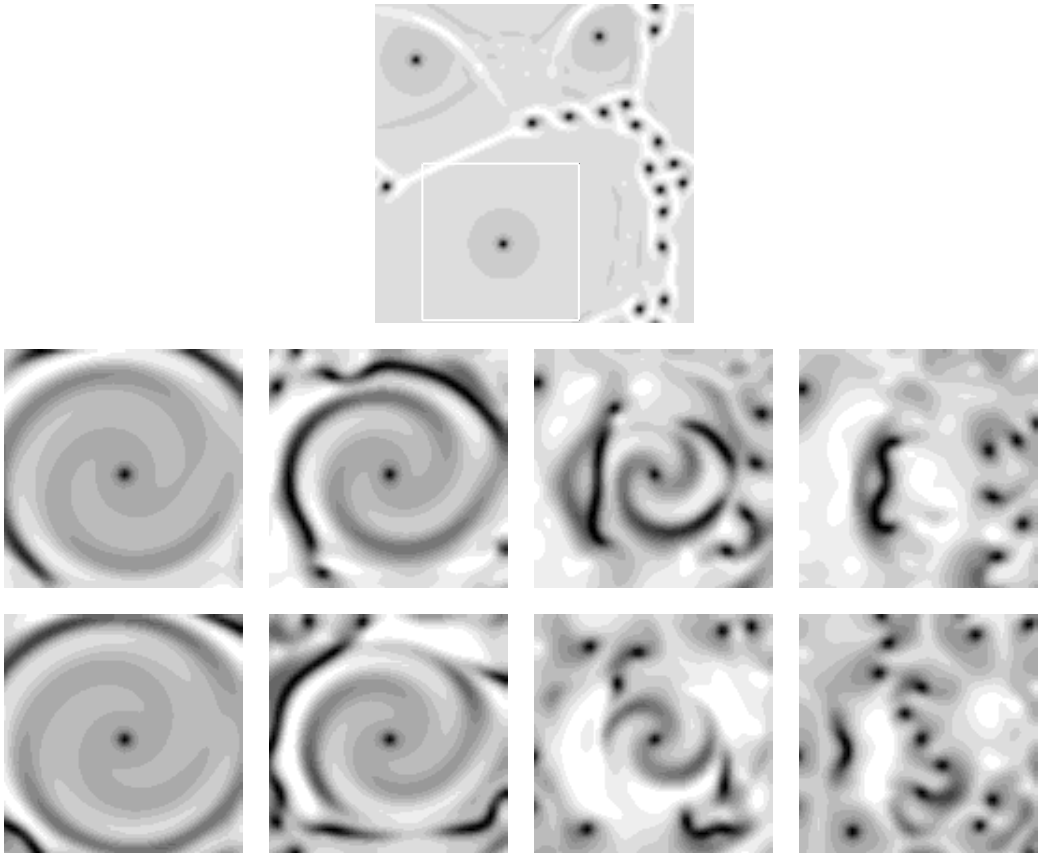

Fig. 8. Annihilation of an argument defect, for $\gamma = 0.3$ and $\kappa = 1.29$. The top figure shows the initial condition generated with $\gamma = 0.1$, the box indicates the domain of the argument defect, and is amplified in the images below. First row: $|A_+|^2$, second row: $|A_-|^2$. From left to right: $t = t_0 + 30$, $t = t_0 + 60$, $t = t_0 + 90$, and $t = t_0 + 120$. At the final stage scalar defects approach the defect core annihilating the n_+ charge.

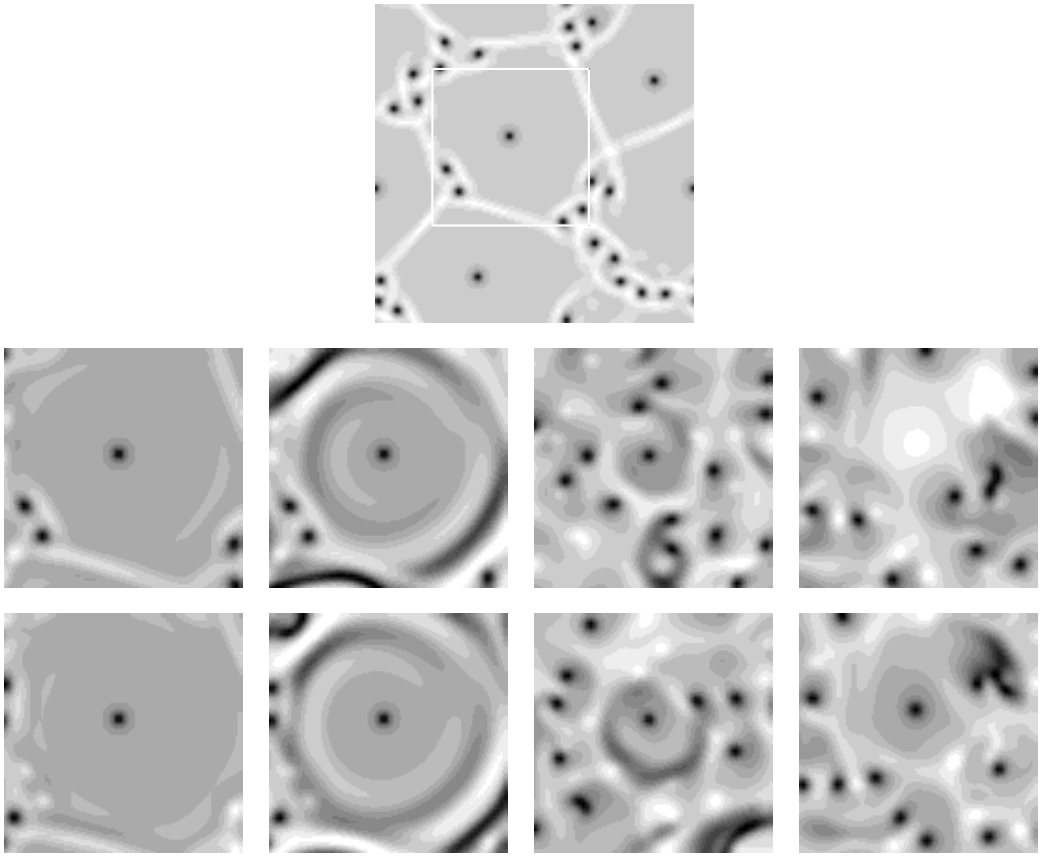

Fig. 9. Annihilation of a director defect, for $\gamma = 0.35$ and $\kappa = 1.29$. The top figure shows the initial condition generated with $\gamma = 0.1$, the box indicates the domain of the director defect, and is amplified in the images below. First row:$|A_+|^2$, second row: $|A_-|^2$. From left to right: $t = t_0 + 50$, $t = t_0 + 100$, $t = t_0 + 200$, and $t = t_0 + 300$. As in the argument defect case, a scalar defect approach at the end the defect core, and annihilate one of the components of the director defect (the one in A_+).

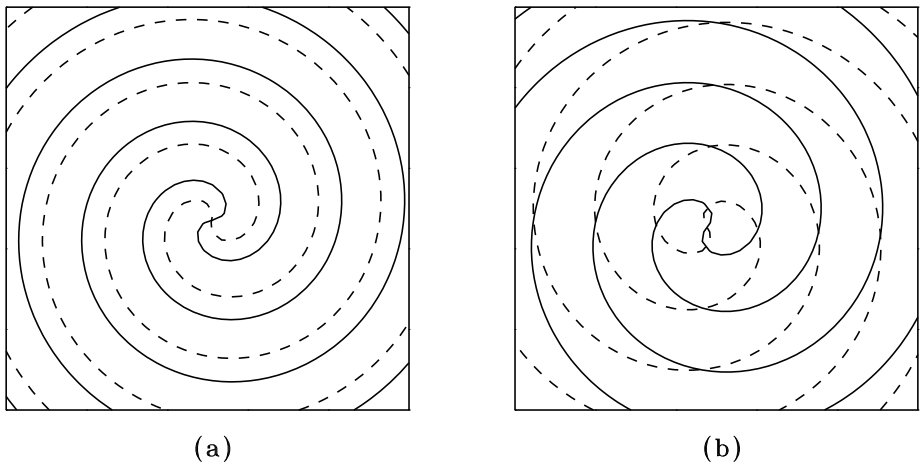

Fig. 10. Lines of constant phase for (a) an argument defect and (b) a director defect. Solid curves correspond to $\phi_+ = 0$ and π, and dashed curves to $\phi_- = 0$ and π. We can see that in (a) $\mathbf{k_R} = 0$ while in (b) $\mathbf{k_R} \neq 0$.

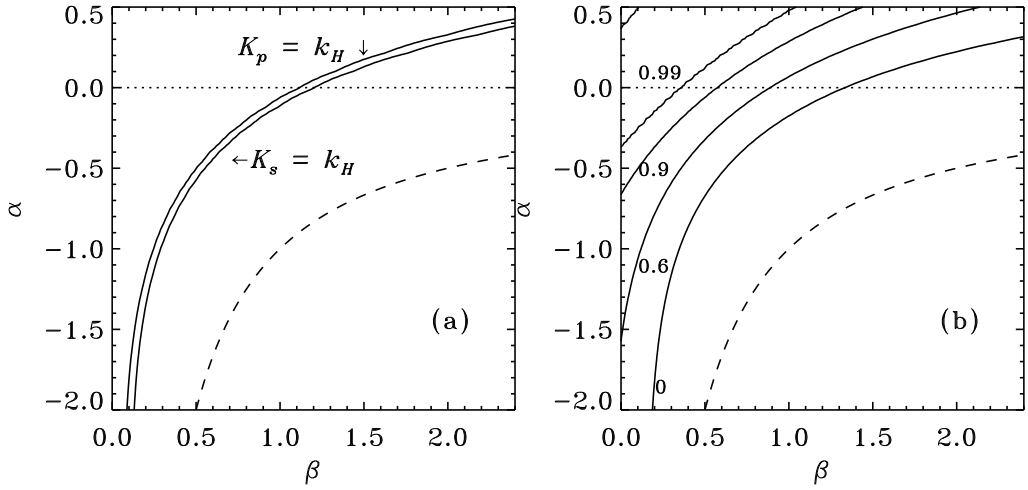

Fig. 11. Stability diagrams in the α-β plane showing different stability regions (the unstable regions are located to the right of the curves). In both figures the dashed curve is $1 + \alpha\beta = 0$. In figure (a) the curves $K_p = k_H$ and $K_s = k_H$ are plotted for $\gamma = 0.3$ (see Eqs. (25) and (22)). The wave emitted by argument defects is unstable to the right of the K_p curve. The wave emitted by director defects is unstable to the right of the K_s curve. In figure (b) we plot the curve $K_p = k_H$ for different values of γ: 0, 0.6, 0.9 and 0.99 as indicated.

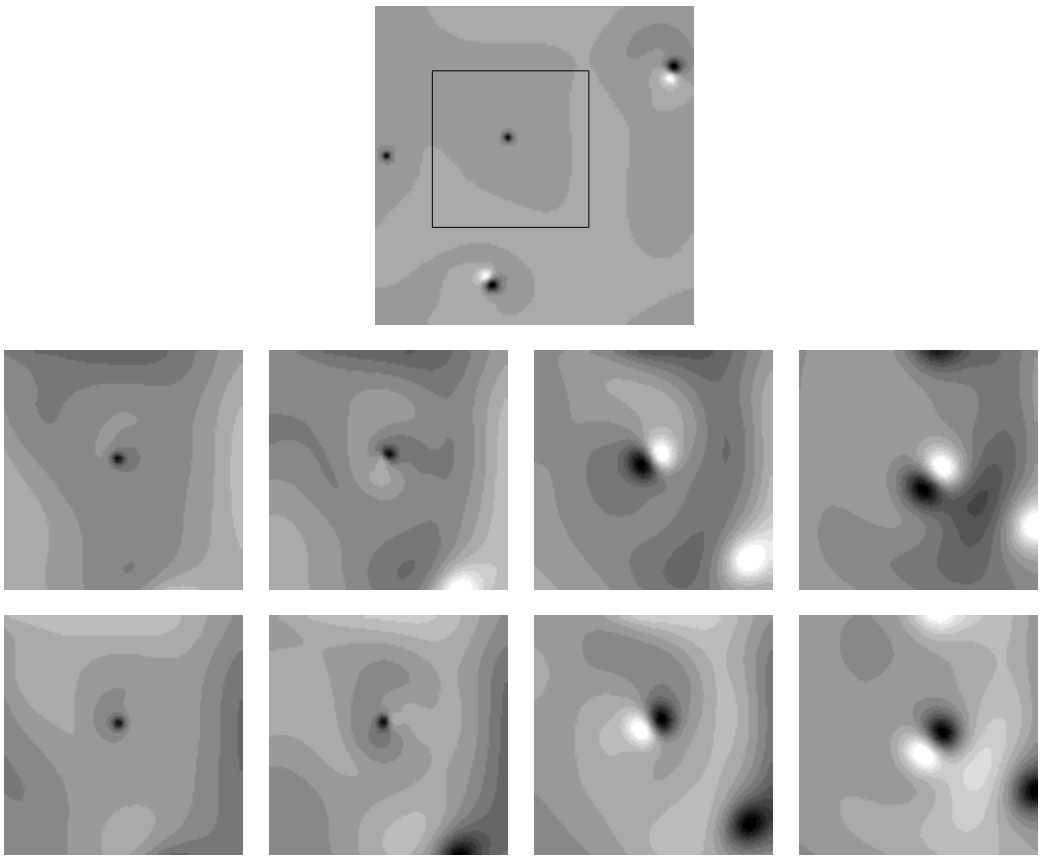

Fig. 12. Splitting of a director defect, for $\alpha = 0.7$, $\beta = 2$ ($\kappa = 0.54$) and $\gamma = 0.95$. The top figure shows the initial condition generated with a value of $\gamma = 0.9$, the square indicates the region amplified in the figures below. In the center of the square there is a director defect. First row: $|A_+|^2$, second row: $|A_-|^2$. From left to right: $t = t_0 + 50$, $t = t_0 + 100$, $t = t_0 + 150$, and $t = t_0 + 200$

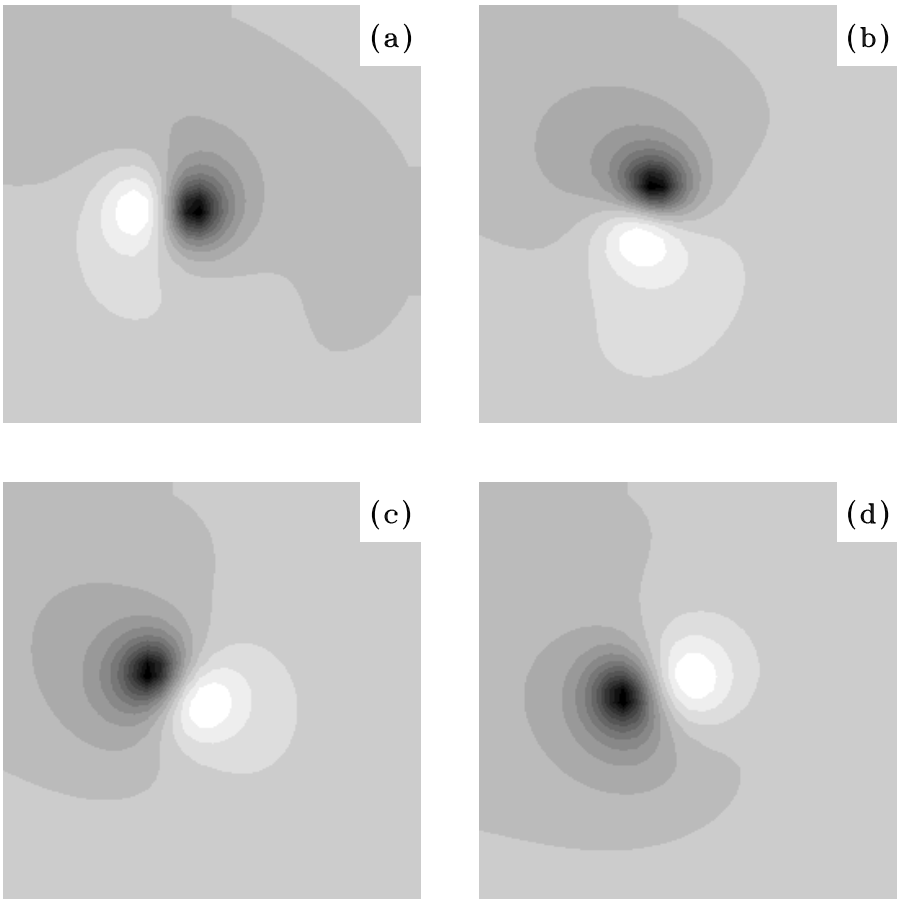

Fig. 13. Time sequence of a bounded pair of scalar defects after splitting of an argument defect, for $\kappa = 1.29$ and $\gamma = 0.9$. The pair rotates and the bounding distance increases with time. The quantity plotted is $|A_+|$ for (a) $t = t_0$, (b) $t = t_0 + 10$, (c) $t = t_0 + 20$, and (b) $t = t_0 + 30$.

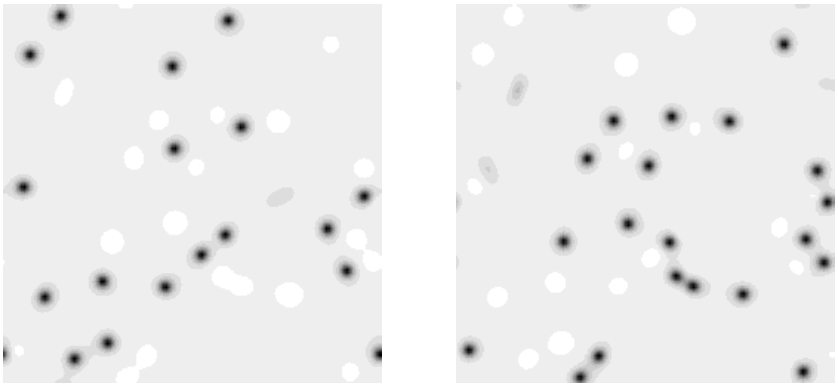

Fig. 14. $|A_+|^2$ and $|A_-|^2$ for $\alpha = 0$, $\beta = 0$ ($\kappa = 0$, potential limit), $\gamma = 0.1$ and $t = 100$ starting from random initial conditions. There is not spontaneous formation of vectorial defects for real coefficients.

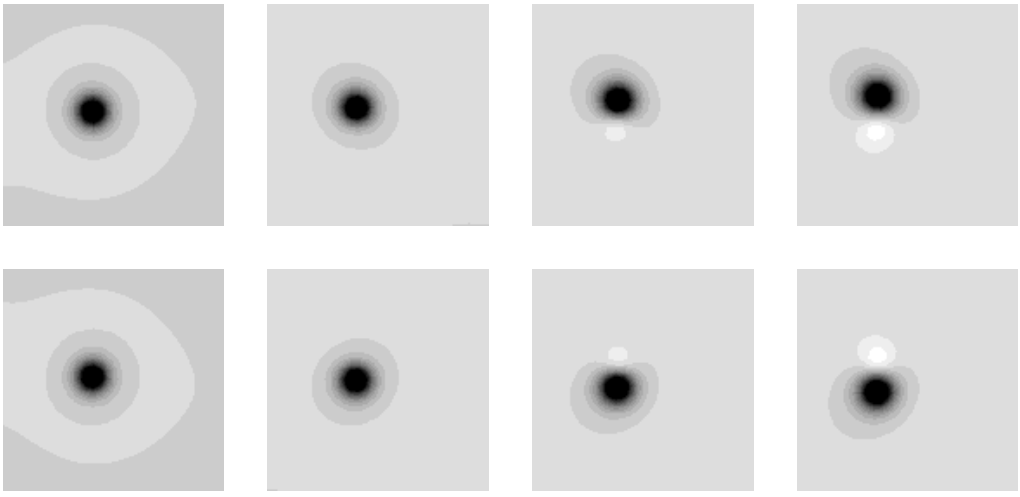

Fig. 15. Temporal sequence showing the splitting of a vectorial defect for real coefficients ($\alpha = \beta = 0$) and $\gamma = 0.2$. First row: $|A_+|^2$, second row: $|A_-|^2$. From left to right $t = 50$, 100, 150 and 200.

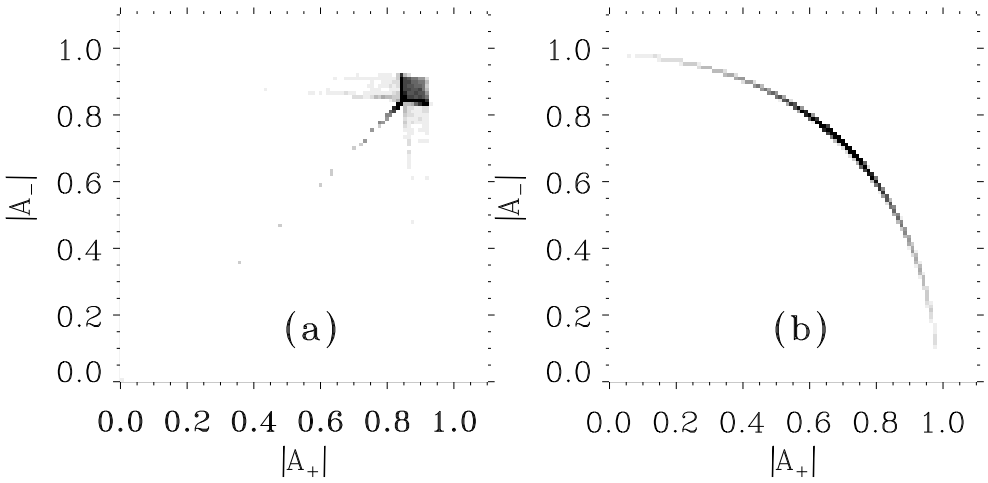

Fig. 16. Joint probability distribution $p(|A_+|, |A_-|)$ for (a) $\gamma = 0.1$ and (b) $\gamma = 0.95$ (in both cases $\kappa = 1.29$). The histograms that are presented in grey levels have been constructed by collecting the values of $(|A_+|, |A_-|)$ at all space points of the simulation domain, and at 100 temporal samples separated by $\Delta t = 1$. The straight diagonal line in the first plot is a signature of the presence of vector defects ($|A_+| = |A_-|$) whereas the curve in (b) displays the anticorrelation between components characteristic of scalar defects.

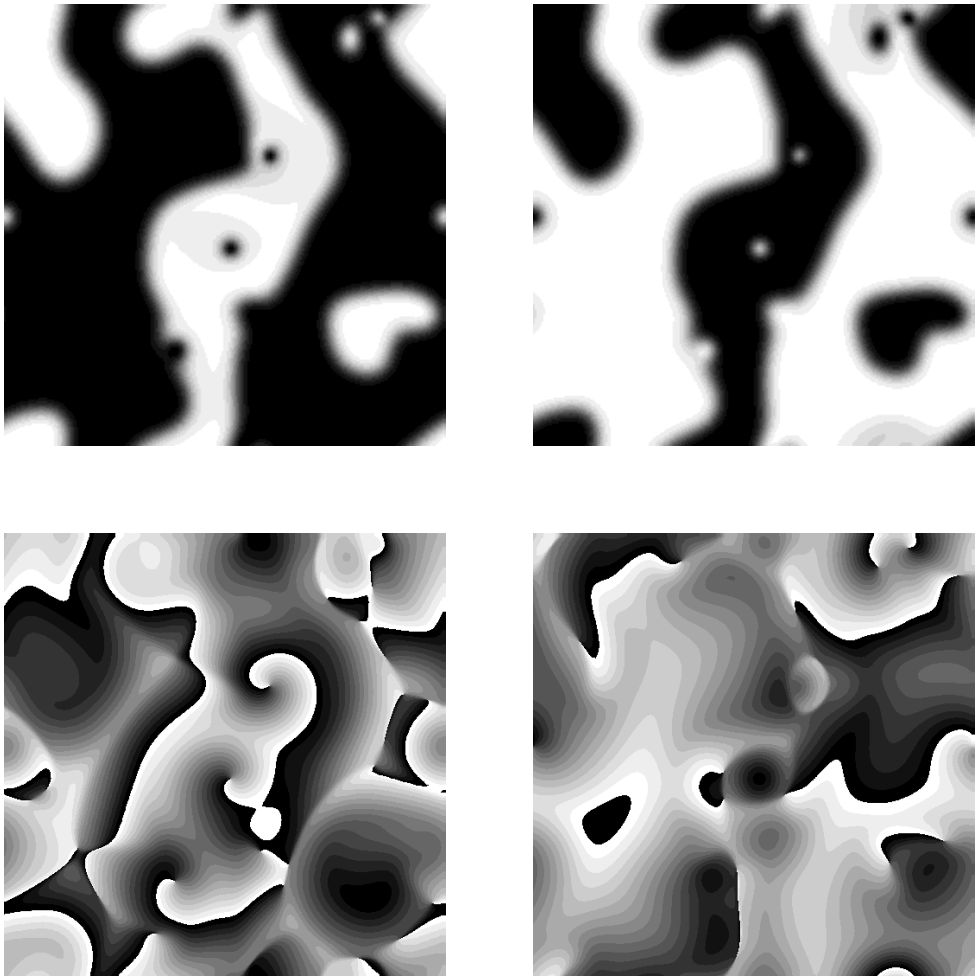

Fig. 17. Configuration of $|A_+|^2$ and $|A_-|^2$ (top row) and the corresponding phases (bottom row) for $\gamma = 1.1$, $\alpha = 0.2$ and $\beta = 2$ ($\kappa = 1.29$), at $t = 50$. The system segregates into two circularly polarized phases, with some defects (the black dots in the amplitude plots, associated to the phase singularities in the phase plots).